Hollow cathode modeling: a first approach on scaling laws

IEPC-2015-14／ISTS-2015-b-14
Presented at Joint Conference of 30th International Symposium on Space Technology and Science
34th International Electric Propulsion Conference and 6th Nano-satellite Symposium,
Hyogo-Kobe, Japan
July 4 – 10, 2015

Gaétan Sary[1], Laurent Garrigues[2], and Jean-Pierre Boeuf[3]

Université de Toulouse ; UPS, INPT ; LAPLACE (Laboratoire Plasma et Conversion d'Energie) ; 118 route de Narbonne, F-31062 Toulouse cedex 9, France.
CNRS ; LAPLACE ; F-31062 Toulouse, France.

A two dimensional quasi-neutral fluid model of an emissive hollow cathode has been developed. It has been coupled with a thermal model into a self-consistent generic model applicable to any hollow cathode design. Important aspects of the model are discussed, including the conservation laws and the treatment of the emissive plasma sheaths. The model is then validated against experimental data for the NASA NSTAR barium oxide cathode (BaO). In light of its good agreement with measurements, we apply the model to another cathode design which uses lanthanum hexaboride (LaB_6) for similar working conditions and a comparative physical analysis of the two cathode designs ensues. We show that the electron current production and heating mechanisms are radically different in the two cathodes: while the behavior of the BaO cathode is predominantly driven by electron emission and bombardment, a major role is played by ionization and ion bombardment in the LaB_6 cathode. The comparative analysis is then extended to a range of electron discharge current and we show that the working point of the cathode does also influence the properties of the plasma and in turn the efficiency and durability of the cathode. The resulting trends might aid the development of new high powered cathode designs.

Nomenclature

e = elementary charge
k_B = Boltzmann's constant
M = atomic mass of Xe
m_e = electron mass
n = plasma density
n_n = neutrals density
$\boldsymbol{u_s}$ = velocity of species s
p_s = scalar pressure of species s
T_s = temperature of species s
$\overline{\boldsymbol{T}}$ = deviatoric viscous stress tensor for neutral species
ϕ = plasma potential

[1] Ph.D. candidate, sary@laplace.univ-tlse.fr
[2] Senior Scientist at CNRS, garrigues@laplace.univ-tlse.fr
[3] Senior Scientist at CNRS, jpb@laplace.univ-tlse.fr

S = plasma production source term
ϵ_{io} = 1^{st} ionization energy of Xe atoms.
$\boldsymbol{j_s}$ = current density of species s
I_e = discharge current
μ_e = electron mobility
Q = xenon mass flow rate
ϕ_{wf} = work function
$SCCM$ = standard cubic centimeter

I. Introduction

Hollow cathodes are critical components of Hall Thrusters (HTs). Since they provide electrons for both the discharge chamber and beam neutralization, the resulting current draw may be quite important and as large as 100 A. With the advent of higher power HTs comes an increasing demand for cathodes capable of supplying large discharge currents. With this goal in mind, it is crucial to study the physics of hollow cathodes, so as to understand the important mechanisms playing a role in the cathode, and in turn to determine scaling laws which might aid the development of new more powerful, more efficient, and more durable cathodes.

Hollow cathodes have been studied extensively both theoretically and experimentally[1–3]. Thanks to this large literature, hollow cathodes using barium oxide (BaO) as an electron emitter are well understood and the region inside the cathode has been numerically modelled with a very high degree of accuracy[4]. Yet, most of these contributions to hollow cathode modelling focus on a single operating point for one cathode design. Only little work has been done to globally describe the influence of design choices and of the operating conditions on the duscharge[5,6].

In this work, we will propose a numerical model of the interior region of a generic hollow cathode. We will put an emphasis on the physical processes that play a role inside the cathode for two different designs and several operating points. After shortly describing our numerical model, we will proceed to its validation against experimental data from diode mode tests of the NASA NSTAR BaO cathode[3]. Important phenomena for this hollow cathode will also be analyzed. We will then apply the model to a different hollow cathode design which uses lanthanum hexaboride (LaB6) as an alternative emitter. The comparison of the discharge properties between the LaB_6 and BaO cathode designs will help us to draw a larger picture showing that hollow cathodes are able to work in different operating regimes depending on their design. We then extend this study to a range of discharge currents and depict how important aspects of the discharge properties for two cathodes with different emitters are affected.

II. Numerical model description

A. General model description

Many hollow cathodes are based upon the same generic geometry (see section II.C and II.E): a hollow tube supports on its interior surface a thermionic emitter insert which emits a large current density of electrons when heated. A set flow of xenon is injected at one end and generates a plasma inside the cathode through collisions with emitted electrons. At the other end, an extraction potential is applied to draw the electron current out. Thanks to this geometry, the heat fluxes resulting from the plasma bombardment maintain the emitter hot enough so that it keeps emitting electrons without requiring an additional heat source. From this important remark, it follows that in order to fully understand the hollow cathode discharge, it is crucial to include both plasma and thermal aspects in a consistent numerical model.

The model is concerned with the description of the plasma in the internal region of the cathode and of the temperature profile in the emissive insert. The 2D-axisymmetric transient plasma fluid numerical model takes into account neutral xenon atoms, single charge ions and electrons. Quasi neutrality is assumed. Hence, plasma sheaths at domain boundaries are treated using a specific model detailed in section II.C. Because of the large densities of neutrals (in excess of $10^{22}\ m^{-3}$), we assume that the plasma is optically thick to radiation at wavelengths close to Xe UV excitation lines[7]. Therefore we limit the effective energy losses caused by inelastic collisions of electrons with neutrals to those related to ionization. Only direct ionization is considered (the influence of metastable xenon will be discussed in a later study). At the cathode walls, we neglect secondary electron emission w.r.t. the large thermionically emitted current densities.

The thermal model is a simple description of the emissive insert and its support tube. The plasma bombardment of the cathode tube carries heat fluxes which are partially lost in electron emission cooling. Black body radiation and conduction to the cathode mount dissipate the remaining energy fluxes.

We now describe important aspects of both the fluid and thermal models.

B. Fluid model

We solve the following fluid conservation laws over the interior region of the cathode. We refer to neutrals, single charge ions and electrons using the indices n, i and e respectively.

- Conservation of neutrals and ions :

$$\frac{\partial}{\partial t} n_n + \nabla \cdot (n_n \boldsymbol{u_n}) = -S \tag{1}$$

$$\frac{\partial}{\partial t} n + \nabla \cdot (n \boldsymbol{u_i}) = S \tag{2}$$

Here S stands for the plasma production source term, which is defined as:

$$S = n n_n \langle \sigma_{io} \boldsymbol{u_e} \rangle = n n_n k_{io}(T_e) \tag{3}$$

The ionizing collision rate coefficient k_{io} is determined from collision cross section data σ_{io} using the Boltzmann equation solver for electrons in weakly ionized gases, BOLSIG+[8]. Cross section data used to calculate collision rates are taken from LXCat website, SIGLO database (www.lxcat.net, retrieved on April 23rd, 2014).

- Conservation of momentum :

$$M\left(\frac{\partial}{\partial_t}(n\boldsymbol{u_n}) + \nabla \cdot (n\boldsymbol{u_n}\boldsymbol{u_n})\right) = -\nabla p_n + \nabla \cdot \overline{\mathbf{T}} + \boldsymbol{R_n} - MS\boldsymbol{u_n}$$
$$\text{, with } \nabla \cdot \overline{\boldsymbol{T}} \cong \mu \left[\nabla^2 \boldsymbol{u_s} + \tfrac{1}{3}\nabla(\nabla \cdot \mathbf{u_s})\right] \tag{4}$$

$$M\left(\frac{\partial}{\partial_t}(n\boldsymbol{u_i}) + \nabla \cdot (n\boldsymbol{u_i}\boldsymbol{u_i})\right) = -ne\nabla\Phi - \nabla p_i + \boldsymbol{R_i} + MS\boldsymbol{u_n} \tag{5}$$

The elastic collision terms appearing in equations (4) and (5) are:

$$\boldsymbol{R_i} = -\boldsymbol{R_n} = nM\nu_{in}(\boldsymbol{u_n} - \boldsymbol{u_i}) \tag{6}$$

where the charge exchange collision frequency of ions with neutrals ν_{in} may be expressed as[2]:

$$\nu_{in} = n_n \sigma_{CEX} \sqrt{\frac{2k_B T_i}{\pi M}} \left[e^{-x^2} + \left(2x + \frac{1}{x}\right) \frac{\sqrt{\pi}}{2} \mathrm{erf}(x) \right]$$
$$\text{, with : } x \coloneqq u_i / \sqrt{\frac{2k_B T_i}{M}} \text{ and } \sigma_{CEX} = 10^{-18} m^2 \tag{7}$$

In (4), μ is the dynamic viscosity of neutral xenon. Temperature dependent data for xenon is available in the literature[9].

We approximate the transport of electrons using drift-diffusion equation:

$$\boldsymbol{j_e} = -en\mu_e \boldsymbol{\nabla}\Phi + \mu_e \boldsymbol{\nabla} p_e, \text{ with } \boldsymbol{j_e} = -en\boldsymbol{u_e} \text{ and } \mu_e = e/m_e \nu_e \tag{8}$$

The total collision frequency for electrons is $\nu_e = \nu_{en} + \nu_{ei}$ where $\nu_{en} = k_{e,n}^m n$ is the elastic collision frequency of electrons with neutrals. We compute the momentum exchange rate $k_{e,n}^m$ in the same way as k_{io}earlier. For the Coulomb collision frequency ν_{ei}, we used the following expression[10]:

$$\nu_{ei} = 4\pi n \ln(\Lambda) \left(\frac{e^2}{12\pi\varepsilon_0 k_B T_e} \right)^2 \sqrt{\frac{8k_B T_e}{\pi m_e}} \tag{9}$$

, with $\ln(\Lambda) \approx 10$ is the Coulomb logarithm.

- Conservation of internal energy:

$$\frac{\partial}{\partial t}\left(\frac{3}{2} p_n\right) + \boldsymbol{\nabla} \cdot \left(\frac{5}{2} p_n \boldsymbol{u_n} + \boldsymbol{q_n}\right) = \boldsymbol{u_n} \cdot \boldsymbol{\nabla} p_n - \frac{3}{2} k_B T_n S - \boldsymbol{u_s} \cdot \boldsymbol{\nabla} \cdot \overline{\boldsymbol{T}} + \boldsymbol{\nabla} \cdot (\overline{\boldsymbol{T}} \boldsymbol{u_s}) + Q_n,$$
$$\text{with } \overline{\boldsymbol{T}} = 2\mu \left(\frac{1}{2} \left((\boldsymbol{\nabla} \mathbf{u_s}) + (\boldsymbol{\nabla} \boldsymbol{u_s})^{\boldsymbol{T}} \right) - \frac{1}{3} (\boldsymbol{\nabla} \cdot \boldsymbol{u_s}) \overline{\boldsymbol{I}} \right) \tag{10}$$

$$\frac{\partial}{\partial t}\left(\frac{3}{2} p_i\right) + \boldsymbol{\nabla} \cdot \left(\frac{5}{2} p_i \boldsymbol{u_i} + \boldsymbol{q_i}\right) = \boldsymbol{u_i} \cdot \boldsymbol{\nabla} p_i + Q_i + \frac{3}{2} k_B T_n S + \frac{1}{2} MS(\boldsymbol{u_i} - \boldsymbol{u_n})^2 \tag{11}$$

$$\frac{\partial}{\partial t}\left(\frac{3}{2} p_e\right) + \boldsymbol{\nabla} \cdot \left(\frac{5}{2} p_e \boldsymbol{u_e} + \boldsymbol{q_e}\right) = \boldsymbol{u_e} \cdot \boldsymbol{\nabla} p_e + Q_e - S\epsilon_{io} \tag{12}$$

In these equations $p_s = \frac{3}{2} n_s k_B T_s$ is the scalar pressure for species s. Thermal conduction fluxes $\boldsymbol{q_s} = -\lambda_s \boldsymbol{\nabla} \mathrm{T_s}$ are computed using thermal conductivities λ_s available in the literature[9,11].

Q_s terms result from heat exchange through elastic collision involving species s. They may be written as:

$$Q_s = \sum_{\alpha \neq s} 3m_s \frac{m_\alpha}{(m_s + m_\alpha)^2} n_\alpha n_s k_{\alpha,s}^m (k_B T_\alpha - k_B T_s) \tag{13}$$

where the summation is carried over all species exchanging momentum. $k_{\alpha,s}^m$ is the elastic collision rate related to species s and α.

Because of the assumed quasi neutrality, we also solve a charge conservation equation to obtain the plasma potential ϕ:

$$\boldsymbol{\nabla} \cdot (\boldsymbol{j_i} + \boldsymbol{j_e}) = 0, \text{ with } \boldsymbol{j_i} = en\boldsymbol{u_i} \text{ and } \boldsymbol{j_e} = -en\boldsymbol{u_e} \tag{14}$$

The plasma potential reference is taken at the electric potential of the metallic walls of the cathode. This results in a potential shift which brings the plasma potential immediately in front of a metallic wall to $\phi = -\phi_{wf}$ i.e. to minus the work function of the material.

C. Fluid domain and boundary conditions

We describe the plasma inside the interior region of the NASA-NSTAR cathode[12], from the inlet boundary upstream to the orifice section where the validity of the fluid approximation becomes questionable. We make use of the cylindrical symmetry of the cathode and reduce the simulation domain to a 2D axisymmetric region (e.g. the upper half of the cathode represented in fig. 1). A constant set flow $Q = 4.25\,SCCM$ of xenon is injected at the inlet following a Poiseuille velocity profile. The pressure at the inlet is set to $20\,Torr$ and the temperature to $300\,K$. At the extraction orifice we set a uniform electron current density so as to extract the desired electron current. It was necessary to assume that electron flow leaves the simulation domain through the orifice with no internal energy in order to obtain a good agreement with experimental data[2]. While this is not satisfactory from a physical standpoint, the basis for such a hypothesis is difficult to investigate in the framework of the present fluid model and will be analyzed in a future work. For ions and neutrals, the exit section of the orifice acts as a non-reflecting boundary. We also set artificially $p_n = 0$ on the orifice boundary as a crude approximation for the free molecular flow expected in the plume of the cathode. Other boundaries are treated as metallic elements and a plasma sheath lies at the boundary.

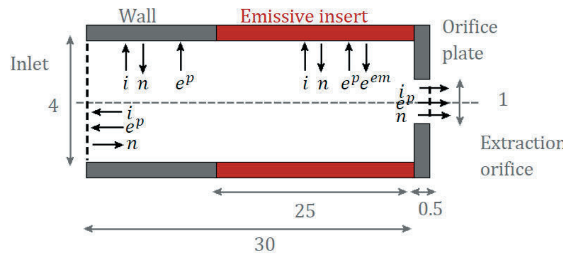

Figure 1. Plasma simulation domain. Dimensions are in mm. Species entering and leaving the simulation domain are labelled n, i, and e which stand respectively for neutrals, ions and electrons.

For materials other than the emissive insert, the sheaths are modelled analytically using the well-known particle fluxes through a sheath resulting from maxwellian electrons and cold ions leaving the plasma:

$$\Gamma_i = n_0 u_B \text{ with } u_B = \sqrt{\frac{k_B T_e}{m_i}}, \text{ and } \Gamma_e^{ab} = \frac{1}{4} n_0 \bar{c_e} \exp\left(-\frac{e\phi_s}{k_B T_e}\right) \text{ with } \bar{c_e} = \sqrt{\frac{8 k_B T_e}{\pi m_e}} \tag{15}$$

where Γ_i and Γ_e are the ion and electron particle fluxes oriented along the normal exiting the simulation domain at wall boundary. ϕ_s is the sheath potential, and n_0 the plasma density.

The resulting energy fluxes carried by ions and electrons are respectively:

$$\Gamma_i^{ab} E_i^{ab} = 5/3\, \Gamma_i^{ab} k_B T_i, \text{ and } \Gamma_e^{ab} E_e^{ab} = \Gamma_e^{ab}(2 k_B T_e + e\phi_s) \tag{16}$$

For non-emissive boundaries we set arbitrarily the work function to $\phi_{wf} \approx 4.6\,V$ as this value is close to the work function of metals such as W or Mo (which are materials commonly used in hollow cathodes[13]). For the emissive material, determination of the work function results from the sheath model which will be described briefly hereafter.

On the interior surfaces, all incoming ions are neutralized and re-enter the domain as neutrals with zero velocity and with a temperature taken as the mean between that of the wall and of incoming ions. In the cylindrical section of the orifice we arbitrarily set that, due to the proximity of the less dense expansion region, 15 % of neutralized ions "bounce" off the wall at high velocity and exit the simulation domain without being re-ionized. This sink term was added to improve the fit to experimental plasma density measurements.

The treatment of emissive sheaths is more complex and it turns out that the physical sheath structure includes a second potential barrier at the wall, with a minimum of plasma potential a few Debye lengths away from the wall. This sheath structure, which results from image-charge effects in the vicinity of the conducting material, is described and modelled in the literature[14]. Originally, only one population of electrons emitted at temperature T_w was considered. Here we complete this 1D sheath description by adding cold ions and maxwellian electrons coming from the plasma region. Physically, the electric potential at the wall, which is obtained as the solution of Poisson's equation, constitutes the barrier which limits the emitted electron current density in Richardson-Dushman law:

$$j_e^{em} = A_0 T_w^2 \exp\left(-\frac{q\phi_{wf}}{k_B T_w}\right), \text{with } A_0 = 120 \times 10^4\ A/m^2 \tag{17}$$

Here j_e^{em} is the emitted electron current density, T_w the local temperature of the emitter, and A_0 a constant independent of the material. ϕ_{wf} is both the effective work function of the emissive material and the height of the potential barrier immediately in front of the wall. Thus, it synthesizes the influence of both the temperature of the wall and of the charge density in front of the wall on the emission process. This is of particular importance in low plasma density situations where the density of emitted electron stops being negligible w.r.t. the density of electrons stemming from the bulk. Consequently, we are able to describe the emission process in both thermionic emission limited regime (taking also into account Schottky effect) and in space-charge limited regime using a single model.

The sheath potential profile is then solved numerically from the wall to the quasi-neutral region (i.e. where the electric field becomes negligible). Because this sheath model cannot be solved analytically, and as it is computationally intensive, the emissive current obtained for a large range of sheath potential, plasma parameters and emitter temperature was tabulated independently from the simulation for the BaO emissive material, using the dependence of the work-function over the temperature[15]. The emitted current density and the effective work function are then interpolated at runtime from these data.

The main strength of this sheath model over pre-existing ones[2], resides its ability to consistently describe the emission limitation in low density regions of the cathodes (e.g. close to the neutral inlet, see section III.A) where we expect that a higher sheath potential is needed to extract a set current density, with respect to denser regions (assuming identical emitter temperatures).

Owing to the porous nature of the BaO-W emissive material[16], it was suggested[4] that the effective emissive surface might be augmented by the sheath penetration between the pores of the emitter, depending on the Debye length (which serves as a rough estimate for the sheath thickness) and on the size and repartition of the pores. Two additional fitting parameters were also needed in this approach to adjust the simulation to the experimentally measured plasma density profile along the axis of the cathode. Here, we choose a simpler approach and uniformly multiply the effective surface of the emissive wall for all particle fluxes by a factor of 3.6 (obtained by fitting the simulation to measurements). While it may seem a large factor, this is lower than the maximum factor used in other models[4], which is as large at 6 in the densest regions. Qualitatively, the main effect on simulation results of this factor is to concentrate the emission process and the plasma in a narrower region. This parameter will remain fixed for all the results shown here for the BaO hollow cathode design.

D. Thermal model

In the thermal simulation, we solve the following heat equation:

$$c_v \frac{dT}{dt} + \boldsymbol{\nabla} \cdot \boldsymbol{q} = S_H \tag{18}$$

where the volumetric heat capacity c_v is set arbitrarily since we are not interested in the transient heating regime and expect short plasma relaxation times w.r.t. to thermal relaxation times. Heat fluxes $\boldsymbol{q} = -\lambda \boldsymbol{\nabla} T$ depend on the thermal conductivities of the materials, as detailed in the following section. At the common boundary with the plasma domain, heat fluxes consistent with the particle fluxes (collected ions and electrons, and emitted electrons) are applied (see equation (19)). During ignition, the heater provides the necessary thermal power to heat the emissive insert. This represented by the heat source term S_H.

E. Thermal simulation domain

Figure 2 describes the simple 2D axisymmetric thermal geometry used for this study. This geometry is based on information available from the literature[3,17] and missing thermal parameters (surface emissivities, conductivities) were either deduced from design data available in the literature[12,13,17] or inferred from the comparison of simulation results to measurements[3]. Table 1 sums up all the thermal parameters involved in these simulations along with the probable material the cathode parts are made of. No dependence of the thermal parameters over the temperature has been included so as to keep the thermal model as simple as possible.

The cathode tube encloses the emissive element and is ended with an orifice plate. On the exterior side of the tube, a heating filament is wound up so as to provide heating during ignition. In the model, the heater is represented as a cylindrical block made of an electrically insulating material. A circular sleeve maintains the emissive insert pressed against the orifice plate. Upstream of the cathode, we set a Dirichlet boundary condition on the wall temperature. Between the emissive insert and the cathode tube, on account of the imperfect thermal contact[12], we set the surface thermal conductivity to $\sigma = 300\,W.K^{-1}.m^{-2}$. For similar reasons, we assume no thermal contact between the sleeve and the emissive insert (insert temperature measurements[3] support well this hypothesis). Outside the cathode tube, a heat shield limits radiative heat losses. We included losses through black body radiation using the emission coefficients given in Table 1.

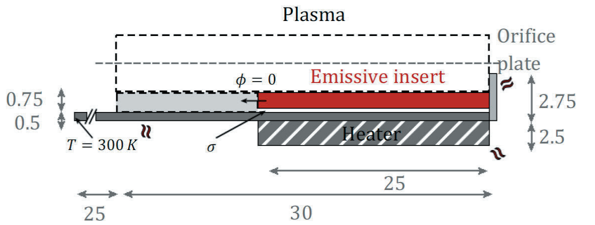

Figure 2. Thermal simulation domain. Dimensions are in mm. Radiative boundaries are figured by wave-like symbols and σ indicates a specified surface heat conductivity.

Cathode Part (Material)	**Thermal conductivity** ($W.K^{-1}.m^{-1}$)	**Radiative transfer coefficient** ε
Tube (W)	110	0.19
Heater (Al_2O_3)	30	0.09
Emissive insert (BaO-W)	65	-
Orifice plate (Mo)	110	0.13

Table 1. Thermal model parameters

Simulation results are mostly influenced by the emissive insert thermal conductivity (which "controls" the temperature gradient amplitude along the insert, see section III.A) and by the radiative transfer coefficient of the heater (since it plays an important role in energy losses because of the large heater surface). The thermal conductivity of the tube mostly sets the minimal temperature of the insert. We do not expect these coefficients to include the full complexity of a real cathode design. However, they show a fair agreement with what is expected from the materials used (e.g. the low conductivity of the insert w.r.t. that of tungsten might come from its porous nature). We also mention that the weak radiative transfer coefficients are a plausible consequence of the heat shields employed in some cathode designs[13].

The coupling of the thermal model with the plasma is realized through heat fluxes. Particles from the plasma bombarding the walls and emitted electrons carry the following heat flux density q_{plasma}:

$$q_{plasma} = -\Gamma_i\left(\frac{1}{2}m_i u_B^2 + e(\phi_s - \phi_{wf})\right) - \Gamma_e^{ab}(2k_B T_e + e\phi_{wf}) + \Gamma_e^{em}(2k_B T_w + e\phi_{wf}) \quad (19)$$

where q_{plasma} is oriented along the normal leaving the thermal domain towards the plasma domain (thus q_{plasma} is positive for an effective cooling of the wall). Γ_i, Γ_e^{ab} are respectively the ion flux and electron flux density collected at the wall. Γ_e^{em} is the emitted electron flux density. In (19), Γ_i, Γ_e^{ab}, and Γ_e^{em} are taken as positive. The flux (19) is the thermal domain boundary condition which couples the thermal model to the plasma bombardment of the walls.

At cathode ignition, a uniform heat source term totaling 45 W is injected in the heater until a stationary temperature profile is obtained, without coupling yet with the plasma simulation. The heater is then turned off and the coupled simulation starts.

III. Results

A. Validation of the model and physical analysis of a discharge in a BaO cathode

Simulation results are now briefly compared with measurements from the literature for the NASA NSTAR BaO cathode at a discharge current of $I_e = 12\,A$ and a flow rate set to $Q = 4.25\,SCCM$. Figure 3 displays a comparison between simulation results and experimental data[3] on the plasma density along the symmetry axis, as well as on the emitter temperature along the surface of the emitter. A close agreement between simulation results and measured quantities for both the plasma density and the temperature of the emitter is observed. Yet, we note a slight discrepancy between simulation and measurements for the position and the width of the peak plasma density, which seems more “diffuse” in our numerical model. As it seems, this difference may be reduced[4] by a local modification of the effective surface of the emitter, owing to sheath penetration in the pores of the emitter (see section II.C). While further tuning thermal and emission parameters might further improve these results, it is also probable that missing physics in the orifice region (such as the unsatisfying internal energy orifice boundary condition for electrons) play an important role experimentally[18] .Consequently we think the design parameters estimated here are sufficiently accurate to realistically compare simulation results with experimental data, within the limits of the physics included in this model.

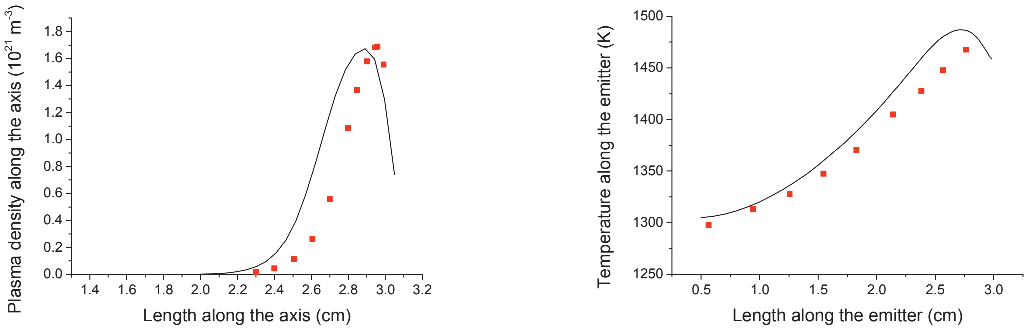

Figure 3. Comparison between plasma density, emitter temperature simulation results (solid line), and experimental measurements for the NASA NSTAR BaO cathode at $I_e = 12\,A$, $Q = 4.25\,SCCM$ (dots). The end of the emitter is located at 3 cm.

We now present in fig. 4 numerical results of the model for the validation reference case (NASA NSTAR BaO cathode with a set mass flow $Q = 4.25SCCM$ and an electron discharge current $I_e = 12\,A$) and propose a detailed physical analysis.

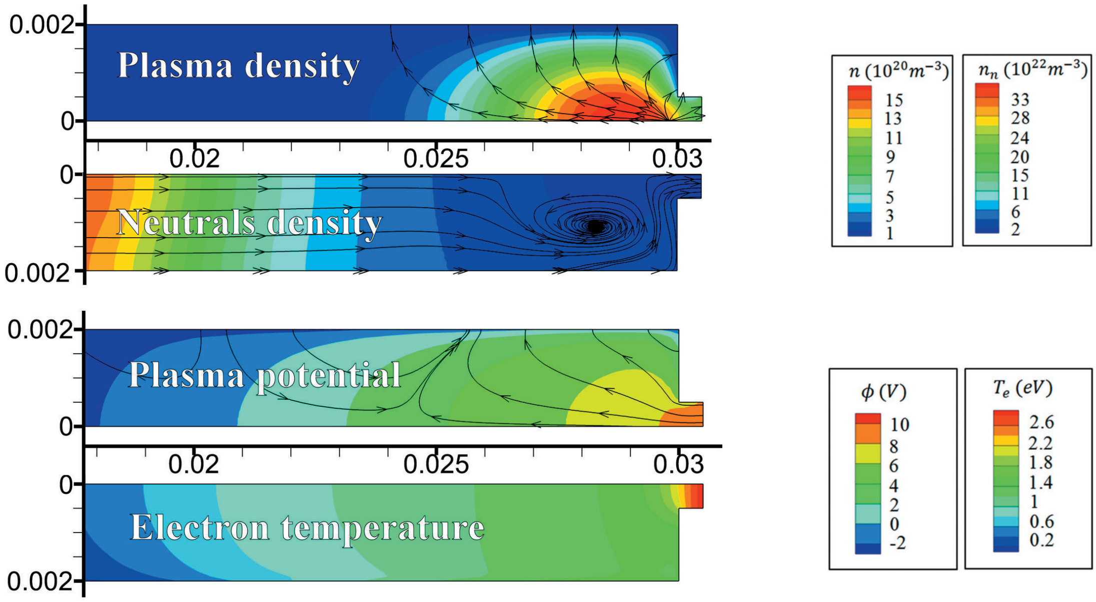

Figure 4. 2D Simulation results for the NASA NSTAR BaO cathode. Plasma density, neutrals density, and plasma potential profiles are overlaid respectively with ions streamlines, neutrals streamlines and electron current lines. The emissive insert is present all along the outer edge of the domain shown here.

These results are qualitatively similar to the ones obtained in other simulation efforts[2,5,19]. The plasma density peaks close to the orifice, where ions are produced. Neutrals flow from the inlet where they are largely unperturbed to the orifice where the influence of the plasma is obvious. There, collisions with ions (through charge exchange) slow down the neutrals and carry ions against the electric field towards the orifice. Because of the large plasma density in this region, and in spite of the low electron temperature, many neutrals are ionized and the resulting ions fall in the plasma sheaths were they are neutralized. Some of the neutralized ions manage to cross the orifice and leave the simulation domain. The plasma potential reaches $10\,V$ (relative to the electrical ground of the cathode) for a discharge current of $12\,A$. The electron current lines coming from the orifice intersect only a small region of the emitter (roughly $5\,mm$ in length), hinting at the fact that only a small region of it is effectively used. This is consistent with the exponential dependence of the emission current towards the temperature (see Richardson-Dushman's law (17)) and with the temperature profile in fig. 3: deeper inside the cathode, the low temperature does not allow for substantial emission. On the contrary, we see that some electron current lines intersect twice the emitter. This shows that, when the net electron current is considered, some regions of the emitter collect more electrons than they emit.

The peak emitter temperature is obtained near the orifice at an axial position close to the maximum of plasma density. While the direct bombardment of the wall plays an important role, the location of the peak emitter temperature also largely depends on the orifice electron energy boundary condition in the plasma domain: since we require that electron flow leaves the domain with no internal energy (see section II.C), the electron temperature rises in the orifice (see fig. 4) and thus increases the electron energy flux to the non-emissive wall section of the orifice. This heat flux reaches then the emitter through thermal conduction. The importance of this heating mechanism was already observed in the literature[5].

A global current balance on the whole cathode shows that, at a set discharge current of $12\,A$, a total electron current of $40.5\,A$ is emitted, while a current of $29.4\,A$ of electrons falls back through the plasma sheaths. We see here that the current balance is dominated by emitted electrons whereas the ionization of the injected xenon plays only a minor role. Because of the low production of ions, we note that only $0.5\,A$ of ion current reaches the walls. Consequently, the energy fluxes heating the insert are carried mostly by electrons: plasma electrons deposit directly on the emissive insert $124\,W$ of heat, whereas ions deposit only $5\,W$ to the insert. $96\,W$ of the total heat flux are lost by emission cooling while the rest is dissipated in radiation and conduction losses.

We now look more closely at the emission process. Figure 5 represents the spatial distribution of current densities on the surface of the insert. This confirms the remarks made earlier about electron current lines: electrons are emitted from a narrow section of the emitter close to the orifice where most of the electron absorption also occurs. While the former comes from the high wall temperature and the locally low work function, the latter is a direct consequence of the high plasma density and of the low sheath potential w.r.t. to the electron temperature in this region (see fig. 4). The impact of the refined emissive sheath model is clearly noticeable in fig. 5: emission models assume usually a simple dependence of the emissive material work function solely on the wall temperature (e.g. a linear relationship[2]). Yet, comparison of the temperature profile in fig. 3 with the work function in fig. 5 at the abscissa 2 cm shows a more complex mechanism plays a role here. A precise analysis of the region away from the orifice (upstream of 2.5 cm in fig. 5) shows that the plasma density and the sheath potential are not sufficient everywhere to draw the electron current. As a result the sheath is in space charge limited regime and a limitation of the emitted current density follows. Therefore, it is clear that the temperature of the material alone is not sufficient to describe the emission process in every region of the cathode.

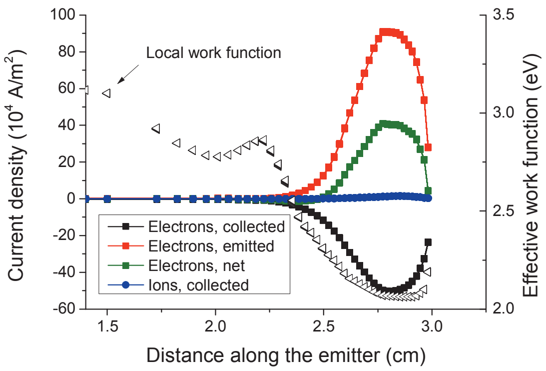

Figure 5. Current densities on the surface of the emissive insert (as defined in (14)) along the normal leaving the plasma domain. The work function as computed by the sheath model is also shown. The end of the emitter and the beginning of the orifice is located at 3 cm.

Though this analysis is satisfying on a physical standpoint, it is true that the role of the refined sheath model is marginal in the global current balance. Yet, it stresses the influence of the plasma density and of the xenon inflow in the discharge. A practical consequence of this is that an attempt at increasing the emitted current density by solely increasing the temperature over some region of the emitter would most probably fail if the plasma were still localized away from the said region.

B. Comparison to a LaB_6 cathode

It is physically interesting to compare the behavior of the cathode detailed in the last paragraph to a cathode using LaB_6 as an emissive element. We first briefly state some general design differences between those two types of cathodes and then analyze the results of the model.

LaB_6 is potential alternative to BaO as an emissive element because of its better resistance to oxygen poisoning and its durability at high current densities[17]. Yet, its work function is somewhat larger: at $T_w = 1500\,K$, we obtain $\phi_{wf}(LaB_6) \approx 2.8\,V$ whereas $\phi_{wf}(BaO) \approx 2.1\,V$. As a result, the emissive element LaB_6 needs to be heated to temperatures sometimes in excess of $2000\,K$ to reach the emission current densities shown in fig. 5 for the BaO cathode. For the LaB_6 emissive element, we assumed no amplification of the emission due to sheath penetration in the pores of the material: because the fabrication process of the emissive layer does not always involve an underlying matrix in the emitter[20], we choose conservatively to consider the emitter surface as flat and homogenous.

Because of the high temperatures needed to obtain a significant electron emission current density in LaB_6 emitters, the cathode design presented earlier (mostly its thermal aspects) is not totally suited for the LaB_6 emissive element. The design we will model for the LaB_6 cathode is based on an existing cathode which is used in conjunction with SNECMA® PPS 1350[21]. This cathode usually supplies discharge currents about a few amperes. We now extrapolate on its design to make it able to sustain electron currents in the order of $12\,A$. Altogether the LaB_6 cathode design remains very similar to figs. 1 and 2 and differs only through its dimensions and thermal parameters: the plasma domain sees its diameter reduced to $2.4\,mm$, the orifice is now $1.2\,mm$ wide, and the domain $1\,cm$ long. The main difference concerning the thermal aspects lies in the improved radiative insulation w.r.t the BaO cathode analyzed earlier, which leads to practically no radiative heat losses apart from the orifice plate (we set $\varepsilon_{orifice\,plate} = 0.3$). The flow rate is set to $Q = 4\,SCCM$ and the discharge current to $I_e = 12\,A$.

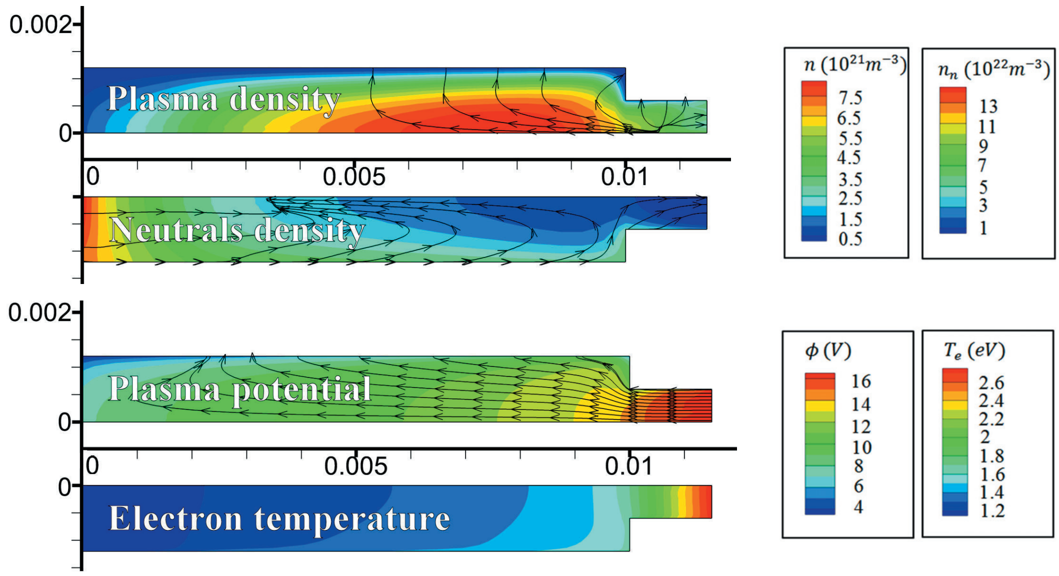

Figure 6. 2D Simulation results for the LaB_6 cathode. Plasma density, neutrals density, and plasma potential profiles are overlaid respectively with ions streamlines, neutrals streamlines and electron current lines.

Simulations results for the LaB_6 cathode shown in fig. 6 display some qualitative differences with the results shown for the BaO cathode (see fig. 4). The plasma in the LaB_6 cathode spreads in the interior of the cathode, alters the neutral flow and depletes them deep inside the cathode. The discharge potential for the LaB_6 cathode is also noticeably larger than for the BaO case ($17\,V$ for the LaB_6 case vs. $10\,V$ for the BaO cathode).

It appears that the emissive insert is used more uniformly here than in the BaO cathode. Electron current lines penetrate deeper inside the cathode w.r.t. the BaO case and reach a larger portion of the LaB_6 emissive insert. Here, the more uniform use of the insert in the LaB_6 cathode is linked with a reduced emitter temperature gradient (surface temperature ranges from $1850\,K$ to $1910\,K$) whereas the gradient in the BaO cathode reached $200\,K$ (see fig. 3). The increased plasma density deep in the LaB_6 cathode also plays its role by allowing for the current extraction.

Joint Conference of 30th ISTS, 34th IEPC and 6th NSAT, Kobe-Hyogo, Japan
July 4 – 10, 2015

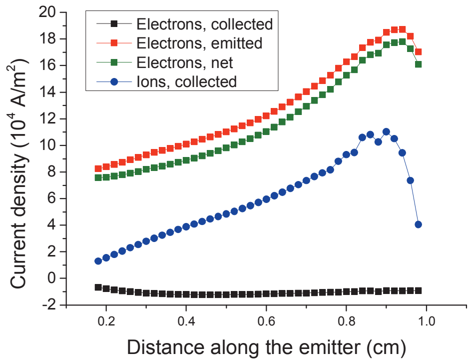

Figure 7. Current densities on the surface of the emissive insert (as defined in (14)) along the normal to the emissive wall. The normal is oriented towards the emitter. The end of the emitter is located at 1 cm.

The current densities in fig. 7 confirm the more uniform electron emission in the LaB_6 cathode. The plasma sheaths are however quite different from the ones in the BaO cathode: here a large current of ions reaches the walls while a very small current of electrons is collected (compare fig. 7 in the LaB_6 cathode with fig. 5. in the BaO cathode). This is caused by the high sheath potentials (on the order of 8 to 10 V in the LaB_6 cathode w.r.t. to 2 V in the BaO cathode) which forbid the relatively cold electrons to reach the wall. A global current balance gives a total emitted electron current of $7.9\ A$, while respectively $1.4\ A$ of electron current and $5.4\ A$ of ion current are lost to the conducting walls. When compared with the required $12\ A$ of electron discharge current, it is obvious that the ionization of the gas plays an important role here, since the net emitted electron current is far from being sufficient to maintain the discharge. We may even say that each neutral Xe atom has to be ionized and neutralized a large number of times inside the cathode since a single ionization event of each incoming neutral (we remind that we set the gas inflow to $Q = 4\,SCCM$) would amount to an equivalent discharge current just under $0.3\ A$. Thus, this cathode regime heavily depends on the neutral density and we easily understand that this can lead at higher discharge currents to ionization instabilities inside the cathode resembling a predator-prey mechanism. Such instabilities have been observed in the present model for small emissive insert radii and large current draws.

From the current balances, it follows that the heating mechanism of the LaB_6 cathode is different from that of the BaO cathode: indeed, we observe that collected electrons carry only $4\ W$ of power by direct impact on the emitter, while $25\ W$ are lost by emission cooling. The needed heating power in the LaB_6 in these operating conditions is almost completely supplied by ions which bring $29\ W$ of thermal energy to the emissive insert. Therefore, the behavior of this cathode is quite the opposite of the one observed for the BaO cathode in section III.A.

In the previous analysis, we did not mention the influence of the geometry. Yet, it is obvious that the radius of the cathode controls the total emitted current and that the width of the orifice of the cathode has to play a role in directing the plasma heat fluxes to the emissive insert. However, much of the physics in the orifice region still needs to be clarified, and as it stands, the assumption that the extracted electrons flux across the orifice boundary carries no internal energy does not allow us to assess the full influence of the width of the orifice. These geometrical effects will be the subject of an upcoming article.

C. Influence of the discharge current – operating conditions

Finally we show how the behavior of the two cathodes described here is affected when the discharge current is modified. The 1st row of fig. 8 shows that, for both cathodes, the discharge potential (i.e. the maximum value of the plasma potential on the exit section of the orifice) passes by a minimum before increasing again at higher discharge currents. At low discharge currents, the increase in discharge potential is linked with the relatively low plasma densities inside the cathode (w.r.t. the case at $I_e = 12\,A$) which lead to an increase in electric field to carry a sufficient electron current density. At higher currents, it may be observed for both cathodes (curve not shown here) that the extracted current which results from the ionization of the xenon increases. Therefore, the concomitant increase in discharge potential may be interpreted as a way to bring more energy to the plasma so as to favor ionization. In between there exists an optimal point for both cathodes at which the discharge potential is minimal. For the BaO design, it also happens to coincide with the minimal contribution of ionization in the total extracted current (not shown here).

BaO cathode LaB$_6$ cathode

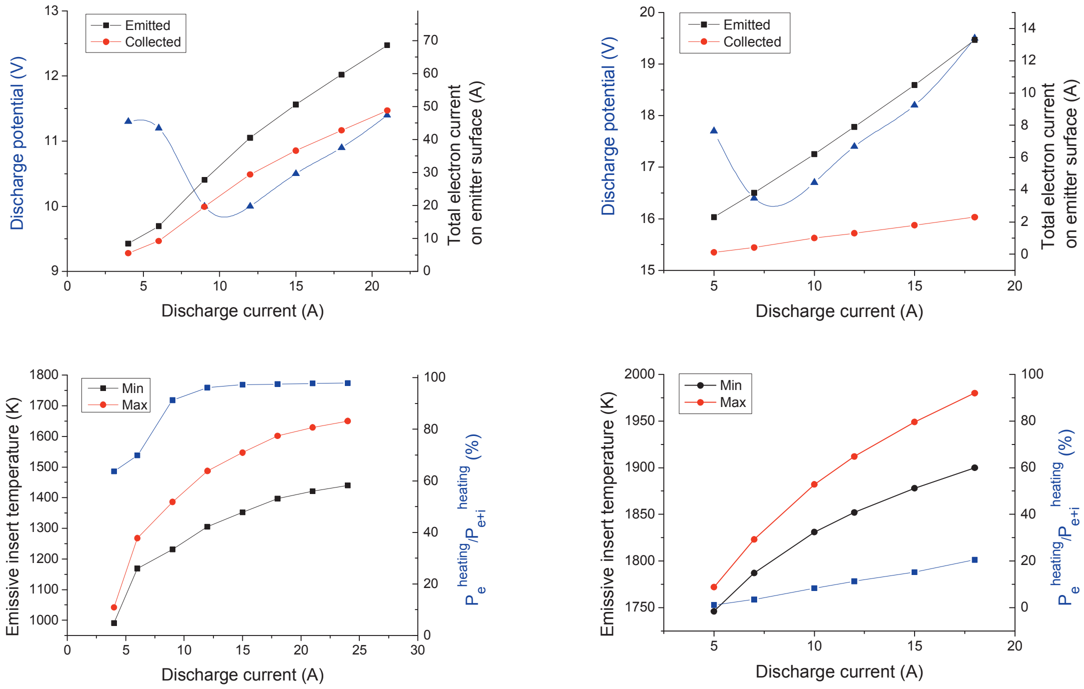

Figure 8. Comparison between the behaviours of the BaO cathode and of the LaB$_6$ cathode on a range of discharge currents. 1st row: current-voltage characteristic and electron current balance. 2nd row: Emitter temperature and emitter heating mechanism (0%: pure ion bombardment heating, 100%: pure electron bombardment heating)

Despite these similarities, there is a sharp contrast between the current balances for the two cathodes: while the discharge current is for the most part supplied by electron emission in the BaO cathode (over 90 % of it stem from the emitter at $I_e \geq 9\,A$), ionisation still plays an important role for the LaB$_6$ cathode over the whole current range in fig. 8 (over 40 % of the electrons come from ionized neutrals at $I_e \leq 18\,A$). The importance of ion bombardment heating of the emitter in the LaB$_6$ cathode is also easily seen in the 2nd row of fig. 8: as the current increases, the temperature of the emitter increases for both cathodes and the LaB$_6$ emitter remains predominantly heated by ion impacts. On the contrary, the heating mechanism of the insert in the BaO cathode switches from a mixed ion-electron bombardment to a heating resulting solely from electron impacts. The pure electron heating seems to be a hallmark of cathodes emitting a very large current on the surface of their insert, well in excess of the collected current. As a practical consequence of these observations, we remark that the insert heating mechanism might also have an influence on the durability of the cathode, as an intense ion bombardment would arguably cause an increased sputtering of the emissive material.

All in all, it may seem that using the LaB_6 emitter is a relatively inefficient solution when compared with the BaO cathode. However we remind that the geometry chosen for the LaB_6 cathode has not been fine-tuned for this particular discharge current. In fact, it is likely that a better choice of the dimensions of the cathode would result in a behavior that is closer to that of the BaO cathode (which was designed for this specific current).

Lastly, we note that due to the increase of the temperature of the emitter with the discharge current (see fig. 8), we anticipate that the LaB_6 emitter could be interesting for cathodes designed for much larger discharge currents ($50 - 100\,A$). In such high current conditions, despite the high work function of the LaB_6 emitter, the high emitter temperature would allow for a large emitted electron current which in turn may be sufficient to obtain a cathode behaving in way similar to the BaO cathode discharge shown earlier at $I_e = 12\ A$.

IV. Summary and perspectives

We have developed a generic model of a hollow cathode for Hall Thrusters which models consistently both the plasma discharge in the interior region of the cathode and the temperature profile of the electron emitter. We first detailed the transient quasi-neutral two dimensional fluid model and some of its important features, such as a physically consistent description of the emissive sheaths which is valid in both space charge limited and thermionic emission limited regimes. We then briefly presented the thermal model and its coupling with the plasma. The simulation results from the coupled fluid-thermal model displays a good agreement with experimental data from a diode mode test of the NASA NSTAR BaO cathode at a discharge current of $12\,A$. A thorough physical analysis of the plasma discharge in this cathode shows that the plasma density peaks in a very narrow region of the cathode and that electron emission plays a predominant role in the total current balance. Emissive insert heating is also mostly the result of electron bombardment. Surprisingly, neutral xenon and ions are bystanders in this discharge and their presence only ensures that the plasma density is high enough so that the emission process can continue without entering space-charge limited regime. We then compared the BaO cathode design to an alternate design using LaB_6 as the emissive element for the same working conditions. We have shown that the global behavior of the LaB_6 cathode differs radically from that of the BaO cathode: the plasma repartition is more spread inside the cathode and the equivalent electron current produced in the ionization of xenon amounts to a large fraction of the total discharge current. The heating mechanism is also different as ion bombardment is responsible for most of the emissive insert heating in the LaB_6 cathode. We anticipate that this regime might have a negative effect on the durability of the cathode as the intense ion bombardment could degrade the emissive insert through sputtering.

Finally, we described how the respective behaviors of the two cathode designs are modified by a variation of the discharge current. Current-voltage characteristics are simulated for each cathode and we show that a minimal discharge potential is obtained at a discharge current depending on the cathode design. The electron production and insert heating mechanisms are affected as well by the electron discharge current. We also observed that the emissive insert temperature and electron emission current increase with the required discharge current. This remark suggests that LaB_6 emitters could be useful in high discharge current cathodes. In such working conditions, LaB_6 emitters would provide a significant emission current density and could operate in an electron dominated regime. As they would not suffer from sputtering due to ion bombardment in these conditions and because of their durability at high temperature, LaB_6 emitters represent strong candidates for future cathodes aiming at discharge currents in the range of 50 to $100\,A$. In a future work, we will further characterize the influence of the designs parameters on the discharge so as draw useful trends for the development of future cathodes.

Acknowledgments

Gaétan Sary benefits from a CNES-Snecma Ph.D. grant.

References

[1] Goebel, D. M., Jameson, K. K., Watkins, R. M., Katz, I. & Mikellides, I. G. Hollow cathode theory and experiment. I. Plasma characterization using fast miniature scanning probes. *J. Appl. Phys.* **98,** 113302 (2005).

[2] Mikellides, I. G., Katz, I., Goebel, D. M. & Polk, J. E. Hollow cathode theory and experiment. II. A two-dimensional theoretical model of the emitter region. *J. Appl. Phys.* **98,** 113303 (2005).

[3] Katz, I., Mikellides, I. G., Polk, J. E., Goebel, D. M. & Hornbeck, S. E. Thermal Model of the Hollow Cathode Using Numerically Simulated Plasma Fluxes. *J. Propuls. Power* **23,** 527–526 (2007).

[4] Mikellides, I. G., Katz, I., Goebel, D. M., Polk, J. E. & Jameson, K. K. Plasma processes inside dispenser hollow cathodes. *Phys. Plasmas* **13,** 063504 (2006).

[5] Katz, I., Mikellides, I. G., Goebel, D. M. & Polk, J. E. Insert Heating and Ignition in Inert-Gas Hollow Cathodes. *IEEE Trans. Plasma Sci.* **36,** 2199–2206 (2008).

[6] Polk, J. E. *et al. Characterization of hollow cathode performance and thermal behavior*. (Pasadena, CA: Jet Propulsion Laboratory, National Aeronautics and Space Administration, 2006).

[7] Malik, A. K., Montarde, P. & Haines, M. G. Spectroscopic measurements on xenon plasma in a hollow cathode. *J. Phys. Appl. Phys.* **33,** 2037 (2000).

[8] Hagelaar, G. J. M. & Pitchford, L. C. Solving the Boltzmann equation to obtain electron transport coefficients and rate coefficients for fluid models. *Plasma Sources Sci. Technol.* **14,** 722–733 (2005).

[9] Bich, E., Millat, J. & Vogel, E. The viscosity and thermal conductivity of pure monatomic gases from their normal boiling point up to 5000 K in the limit of zero density and at 0.101325 MPa. *J. Phys. Chem. Ref. Data* **19,** 1289 (1990).

[10] Oudini, N., Hagelaar, G. J. M., Boeuf, J.-P. & Garrrigues, L. Physics and modeling of an end-Hall (gridless) ion source. *J. Appl. Phys.* **109,** 073310 (2011).

[11] Braginskii, S. Transport processes in a plasma. *Rev. Plasma Phys.* **1,** 205 (1965).

[12] Katz, I., Polk, J. E., Mikellides, I. G. & Hornbeck, S. E. Combined plasma and thermal hollow cathode insert model. in *The 29th International Electric Propulsion Conference (IPEC), Princeton, NJ, October 31-November 4, 2005* (Pasadena, CA: Jet Propulsion Laboratory, National Aeronautics and Space Administration, 2005., 2005). IEPC-2005-228

[13] Warner, D. J. *Advanced cathodes for next generation electric propulsion technology*. (DTIC Document, 2008).

[14] Lin, T. & Eng, G. Thermionic emission including both space-charge and image forces. *J. Appl. Phys.* **65,** 3205–3211 (1989).

[15] Cronin, J. L. Modern dispenser cathodes. *IEE Proc. Solid-State Electron Devices* **128,** 19–32 (1981).

[16] Aida, T. *et al.* Emission life and surface analysis of barium-impregnated thermionic cathodes. *J. Appl. Phys.* **74,** 6482 (1993).

[17] Chu, E. & Goebel, D. M. High-Current Lanthanum Hexaboride Hollow Cathode for 10-to-50-kW Hall Thrusters. *IEEE Trans. Plasma Sci.* **40,** 2133–2144 (2012).

[18] Mikellides, I. G., Katz, I., Goebel, D. M. & Jameson, K. K. Evidence of nonclassical plasma transport in hollow cathodes for electric propulsion. *J. Appl. Phys.* **101,** 063301 (2007).

[19] Mikellides, I. G. & Katz, I. Wear Mechanisms in Electron Sources for Ion Propulsion, I: Neutralizer Hollow Cathode. *J. Propuls. Power* **24,** 855–865 (2008).

[20] Palluel, P. & Shroff, A. M. Experimental study of impregnated-cathode behavior, emission, and life. *J. Appl. Phys.* **51,** 2894 (1980).

[21] Bugeat, J. Oxide Hollow Cathode Assembly for PPS1350. *Eur. SPACE AGENCY-Publ.-ESA SP* **465,** 595–600 (2000).